

Contents lists available at ScienceDirect

Cryogenics

journal homepage: www.elsevier.com/locate/cryogenics





Electromagnetic-thermal finite element model coupled to reduced electrical circuit for simulating inductive HTS coils in overcurrent regimes

Gabriel Hajiri ^a, Kévin Berger ^{a,*}, Frederic Trillaud ^{a,b}, Jean Lévêque ^a

- a Université de Lorraine, GREEN, F-54000 Nancy, France
- ^b Instituto de Ingeniería, Universidad Nacional Autónoma de México, Ciudad de México, Mexico

ARTICLE INFO

Keywords:
Coupling FEM
Circuit
Multiphysics FEM
Overcurrent
Quench
REBCO
T-A formulation

ABSTRACT

To improve the understanding of the behaviour of High Temperature Superconducting (HTS) devices in electrical systems, it is relevant to couple Finite Element (FE) Models (FEM) and Electrical Circuits (EC). This coupling should include enough physics to look justly at the impact of the devices on the electrical system. Since some devices require the full or partial transition of the superconductor to its normal-resistive state, such as fault-current limiters, for instance, their modelling must address the dynamic change that the superconductor experiences moving both ways between its superconducting state and its normal-resistive state. To tackle this challenge, a multiphysics FEM coupled to an EC has been built targeting overcurrent operations of 2G HTS coils, used in such devices. Here, the basis of the approach is the electromotive force to compute the magnetic induction in the coil. The FEM is composed of two coupled submodels, an Electromagnetic one (EFEM) implementing the T-A formulation and a Thermal one (TFEM). The resulting TEFEM is coupled to an Electrical Circuit Model (ECM) in the same FE solver yielding the TEFEM – ECM. To further improve the computation time, a reduction method is employed to skim the ECM, without sacrificing accuracy. The simulation results for the most reduced version of the model are compared with experimental data obtained in liquid nitrogen at 77 K for a current pulse discharge system connected to a 2G HTS coil, showing good agreement.

1. Introduction

There is a growing interest in building coupled Finite Element (FE) Method - Circuit models to simulate superconducting devices interacting with electrical systems [1-4]. On one hand, the advantage of using FE analysis is found in the physical and geometrical details that the tool provides in comparison to lumped-parameter models. It is particularly relevant when looking at the performance of the superconductor within the device itself considering the non-linearity of the superconductor under the presence of field and temperature change [5]. On the other hand, the circuit model is ideal to model complex electrical system made of several components such as generators, power converters, cables, transformers and any power equipment found in modern power grids. If the circuit model is relatively simple (a few of equipment), the main tendency is to construct such coupled models in the same numerical tool [6–9]. The coupling is then direct and the circuit equations are solved alongside the FEM equations. Hence, the superconductor is often represented in the circuit as an electrical impedance, where the dependence of the electrical resistance on the transport current and

temperature are taken into account [10–13]. The inductance is then derived from the integral of the derivative of the magnetic vector potential [7]. It is expected that such an approach would bring more accuracy in the modelling of superconductors as part of a more complex electrical network.

Recent works have been mainly dedicated to evaluate the FE — Circuit coupling when the transport current is lower than the critical current. In this sub-critical condition, the models are useful for estimating the hysteresis losses of the superconductor [14,15]. However, for some HTS devices such as fault-current limiters, it is necessary to simulate the dynamic of the superconductor beyond its critical current [16,17]. For such application, the superconductor enters a transition where the superconductor fully or partially quenches. As the current goes beyond the critical current, a thermal runaway may result for prolonged transitions [18–22]. In this context, a model relying on a parallel electrical circuit composed of the superconductor and its surrounding metallic layers has been developed in [23] for a purely resistive HTS component considering a single REBCO tape. This work targeted the modelling of resistive fault-current limiters in which equipment see overshoot of the current in transients either in alternating

E-mail address: kevin.berger@univ-lorraine.fr (K. Berger).

^{*} Corresponding author.

NT	.1	0	Cristical transportunity (II)
Nomen	ciature	θ _c CuB	Critical temperature (K)
	Magnetic vector potential (Wb m ⁻¹)		Index representing the bottom copper layer
A		CuT	Index representing the top copper layer
В	Magnetic flux density (T)	Sub	Index representing the substrate
C	Capacitor (F) Electrical field (V m ⁻¹)	sc	Index representing the superconducting layer
E	Critical electrical field equal to 10^{-4} (V m ⁻¹)	nc	Index representing the superconducting layer when the
E _c	*		superconductor temperature is higher than its critical
ECM	Electrical Circuit Model		temperature θ_c
H	Magnetic fields (A m ⁻¹)	ρ	Electrical resistivity (Ω m)
\mathbf{H}_1	Magnetic field vectors in the upper region of the		- ECM Fully coupled EFEM - ECM - TFEM
	superconducting layer (A m ⁻¹)	TFEM	Thermal FE model
\mathbf{H}_2	Magnetic field vectors in the lower region of the	EFEM	Electromagnetic FE model
	superconducting layer (A m^{-1})	$B_{//}$	Magnetic flux density parallel to the (a, b) plane of the HTS
I	Current (A)	_	tape (T)
$I_{\rm c}$	Critical current defined at E_c (A)	$B\bot$	Magnetic flux density perpendicular to the (a, b) plane of
J	Current density (A m ⁻²)		the HTS tape (T)
l	Length of the superconducting coil (m)	m	Index representing each conductive layers of the tape
L	Inductance (H)	$k_{ m f}$	Anisotropy factor
L_{load}	Inductance of the conventional coil (H)	β	Constants that characterize the variation of I_c vs B
n	Index of $E(J)$ power law	φ	Magnetic flux (Wb)
r	Coordinate in the radial direction (in index, means	B_0	Constants that characterize the variation of I_c vs B (T)
	component along r) (m)	i	Index representing each layer of the tape
$R_{ m load}$	Resistance of the conventional coil and the electric cable	j	Index representing each turn of the coil
	(Ω)	n	Normal unit vector
S	Cross section (m ²)	J_c	Critical current density (A m ⁻²)
T	Current vector potential (A m ⁻¹)	$J_{ m c0}$	Critical current density at zero applied magnetic field (A
th	Thickness (mm)		m^{-2})
U	Voltage (V)	t	Time (s)
$U_{ m c}$	Capacitor voltage (V)	q	Losses per volume unit (W m ⁻³)
$U_{ m c0}$	Capacitor voltage at $t = 0$ (V)	q_0	Surface heat flux (W m ⁻²)
$U_{ m coil}$	Voltage of the superconducting coil (V)	U_R	Resistive voltage of the superconducting coil (V)
V	Volume (m ³)	U_L	Inductive voltage of the superconducting coil (V)
Z	Coordinate in the axial direction (in index, means	C_p	Specific heat (J kg ⁻¹ K ⁻¹)
	component along z) (m)	μ_0	Magnetic permeability (H m ⁻¹)
γ	Density (kg m $^{-3}$)	k	Thermal conductivity (W $m^{-1} K^{-1}$)
θ	Temperature (K)	w	Tape width (m)

current or direct current applications [24]. A more general approach to simulate HTS tapes in an arbitrary current range has been proposed in [25] where the electrical equations coupled with the thermal equations are calculated and solved in the form of ordinary differential equations and differential algebraic equations in the case of a voltage source and a current source, respectively. In such works, modelling the transition of the superconductor from its superconducting state to its normal-resistive state as well as the recovery of its initial condition has been the main issue. Indeed, these are critical aspects of catching the actual behaviour of fault-current limiters in transients. The present paper intends to address such a challenge proposing the modelling and coupling of an electromagnetic-thermal Finite Element Model (TEFEM) with an Electrical Circuit Model (ECM) of 2G HTS coils used in such devices. In order to do so, the present work should address three issues. Firstly, the methodology should be extended to the modelling of inductive coils found in power components such as inductive fault-current limiters and transformers and to some extent cables (twisted tape on a former), thereby extending the range of applications. These coils are more complex to simulate than non-inductive (purely resistive) configurations. Here, the proposed approach deals with the notion of electromotive force rather than inductance to maintain a high level of accuracy. The second issue is to simulate the behaviour of a superconducting coil under overcurrent conditions that imply the modelling of the current sharing across the different layers of the HTS. This is essential to better understand the thermoelectric operation of 2G HTS tapes in transients. The third issue is to simplify the model of the coil's electrical circuit to

reduce further the computational cost. It is done by identifying the ideal model that combines low computing resources and good accuracy. This objective is attained via a model reduction. Finally, having addressed all those previous issues with the proposed coupled TEFEM-ECM, the results of simulation of an actual experiment involving a 2G HTS coil submitted to current pulses of various amplitudes at 77 K in liquid nitrogen (LN2) are compared with experimental data, thereby validating our approach.

This paper is divided into five sections beside the introduction (section 1) and the conclusion (section 7). The section 2 presents the characteristics of the commercial REBCO tape used to wind the inductive coil. The salient parameters of the latter are provided. The tape and coil were characterized in LN2 at 77 K to infer their *n* index and critical current I_c . The section 3 details the experimental setup of the overcurrent facility providing the electrical schematic implemented in the circuit model. The section 4 presents the coupling between the EFEM, the TFEM and the ECM referred to as the TEFEM - ECM. The section 5 constitutes the core of this work introducing the reduction of the ECM. Different ECM are detailed from the most accurate model to the retained one which is expected to yield an accurate account of the circuit behaviour of the coil. The final TEFEM - ECM is validated against experimental measurements in section 6. The main results of the present work are summarized in the conclusion arguing that the simplifications introduced by the model reduction and the electromotive force allows to significantly decrease the complexity of simulating HTS inductive coils keeping a fair accuracy on their current and voltage response to

transients. It opens a path to accurately simulate inductive components in power systems such as inductive fault-current limiters and transformers, for instance.

2. REBCO tape and coil

In this section, the characteristics of the commercial REBCO tape supplied by Shanghai Superconductor Technology Co., Ltd and the coil wound with it are presented. Fig. 1 shows a micrograph of the tape having a width of 4 mm, a total thickness of about 93.7 μm : 21.9 μm of copper at the top, 1.3 μm of silver, 3.5 μm of YBaCuO, 49.3 μm of substrate, and 17.7 μm of copper at the bottom.

The coil is made of 6 turns of REBCO tape co-wound with a paper insulator (100 μm thick). The coil was wound on a 3D printed plastic former which was screwed on a G-11 support. The winding tension is loose allowing a relatively good wetted surface of the tape despite the presence of the turn-to-turn insulation. The inner diameter of the coil is 120 mm. Fig. 2 shows the coil configuration.

To avoid the movement of the tape during the current discharge, the coil was partially glued on its support. The tape was soldered over 6.5 cm of its length to Cu sheets for a contact area of about 65 mm \times 4 mm. As shown in Fig. 2, these Cu sheets are extended by Cu braided cables that are themselves connected via power cables to the power source for DC tests or to the current pulse discharge circuit for the overcurrent tests. A pair of voltage taps, 2.26 m apart, were soldered on the tape to monitor the coil voltage.

A short sample and the coil were characterized in LN2 at 77 K. The short sample is from the same batch as the one used to wind the coil. For the short sample test, pressed Cu contacts allowed to feed the tape with current. For the coil tests, the Cu braided terminals of the coil were connected directly to the DC power supply. This power supply, controlled by a function generator, provided automatic discrete steps of increasing current. The step setting is 5 A up to a current of 100 A followed by steps of 0.5 A from 100 A to the current corresponding to the maximum voltage set by the user. At the maximum voltage measured across the tape, the current is ramped down. An average value over 100 measured voltages was recorded by a nano-voltmeter for each current increment. The results are gathered in Fig. 3. It shows the *E-I* curves for both the short sample and the coil. The coil voltage $U_{\rm coil}$ is rescaled to the electrical field E assuming that $U_{\text{coil}} = E \times l$ with l the distance between the voltage taps along the coil. The short sample has a critical current I_c equal to 138.5 A and an index of transition n equal to 22, whereas the coil has a lower critical current of 114.5 A and an n index equal to 21.5, about the same as the short sample. This discrepancy results from the strong sensitivity of the critical current on the magnetic field at low field leading to a reduction of 17 %. The *n* value is miscellaneously impacted with a loss of 2 % in its value. Table 1 summarizes the data obtained for the short sample and the coil.

The measured critical current I_c and index of transition n of the coil

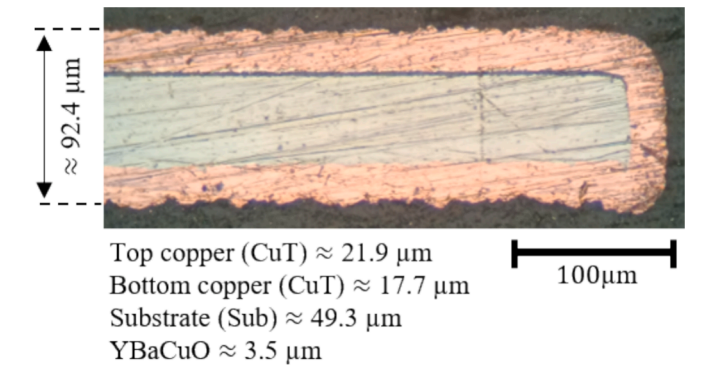


Fig. 1. Microscopic view and geometrical dimensions of the REBCO tape supplied by Shanghai Superconductor Technology Co., Ltd.

(a)

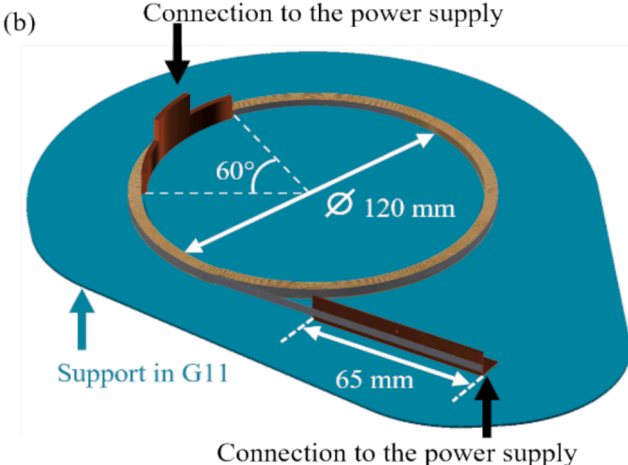


Fig. 2. (a) Picture of the superconducting coil, (b) drawing showing the different geometric parameters of the coil.

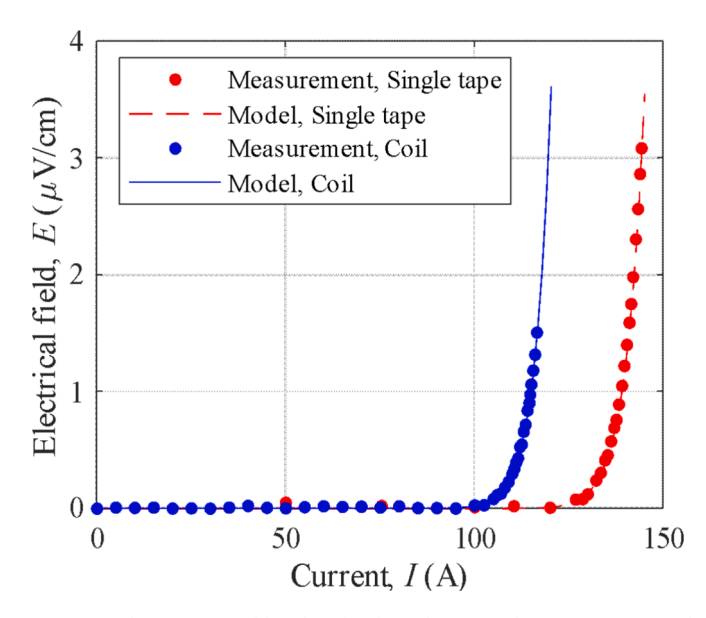


Fig. 3. *E-I* characteristics: blue dots for the inductive coil in LN2 at 77 K and red dots for a short sample (same batch as the coil). The coil voltage $U_{\rm coil}$ is replaced by the electrical field E to fit the results on the same graph. It is assumed that $U_{\rm coil} = E \times l$, with l the distance between the voltage taps. (For interpretation of the references to colour in this figure legend, the reader is referred to the web version of this article.)

are subsequently used in the power law model which is employed to infer the resistivity of the superconductor in the EFEM (see section 4.2). In terms of the electric field E, the power law reads [26],

Table 1
Characteristics of the REBCO tape and the coil.

onaracteristics of the ranges tape that the con-				
20 cm				
138.5 A				
22				
2.26 m				
114.5 A				
21.5				
6				
120 mm / 124.5 mm				

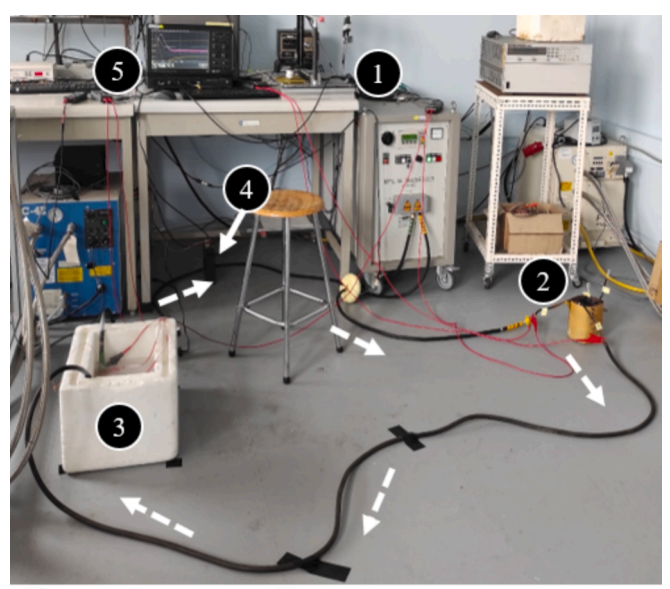
$$E = E_c \left(\frac{I}{I_c}\right)^n \tag{1}$$

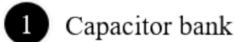
with $E_c = 1 \mu V/cm$ and I the current.

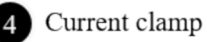
3. Experimental setup for overcurrent tests

The experimental setup for the overcurrent tests, shown in Fig. 4, is composed of the capacitor bank "CB" (1), a Cu inductive coil of 2.5 mH and 0.4 Ohm (2), the REBCO coil in its cryostat (3), a current clamp to measure the current (4), and an oscilloscope with a differential probe to record the voltage $U_{\rm coil}$ across the REBCO coil (5). This experimental setup is modelled as an electrical circuit in the TEFEM — ECM (see Fig. 5).

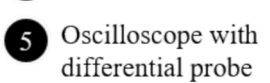
The specific discharge setup is made of a capacitor bank CB (Impulse Magnetizer K-Series) that can supply up to 10 kJ (2 kV - 25 kA). Its equivalent capacitance is 5 mF. The CB is connected to the network converting the AC voltage from the network to a DC voltage. Since the current shape is defined by the load, a Cu inductive coil is added in series with the HTS coil to add an extra impedance in the circuit. The magnitude of the total inductance defines the value of peak current and the discharge time. In the present case, the peak current ranges from $I_{\rm C}$ to







2 Resistive coil



3 REBCO Coil + Cryostat

Fig. 4. Picture of the discharge setup for over-current tests.

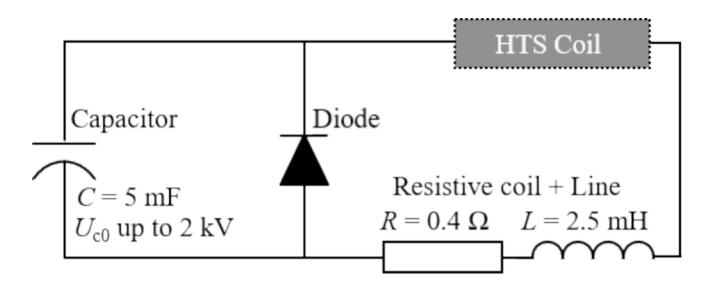


Fig. 5. Schematic drawing of the electrical circuit simulating the experimental setup. The parameters of the discharge system are provided by the manufacturer and the parameters of the coil were experimentally measured.

 $5.6 \times I_{\rm c}$, $I_{\rm c}$ being the measured critical current of the coil given in Table 1. By controlling the peak current via the inductance of the system, the HTS coil can be protected. Thus, the setup guarantees that the HTS coil does not experience any extreme values of current (up to $25\,{\rm kA}$) supplied by the CB. The diode is used to block the negative voltage on the CB and allows the current to flow freely. Not shown in Fig. 5, a $30\,{\rm kA}$ -class thyristor controls the discharge of the equivalent capacitance C whereas the charge is performed via another switch.

4. Modelling and coupling between the electromagnetic-thermal finite element models and the electrical circuit model

4.1. Overview of the TEFEM - ECM

In this section, we aim to describe the complementarity between the different physics used, as well as the complete coupling between the FE model and the ECM. Fig. 6 shows the complete TEFEM - ECM with exchanged variables. It is made up of three submodels corresponding to EFEM, TFEM and ECM. The first one is the Electromagnetic FE submodel (EFEM) which makes use of the full **T-A** formulation. The **T-A** formulation was chosen over other classical formulations, such as the **H** formulation, to build an EFEM that is accurate and fast in terms of computation time [15]. However, it should be noted that recent studies have shown the **J-A-** Φ formulation can be considerably faster for HTS coils in 2D [27]. The magnetic flux density **B** is computed in the whole domain from the magnetic vector potential **A** as $\mathbf{B} = \nabla \times \mathbf{A}$ and the

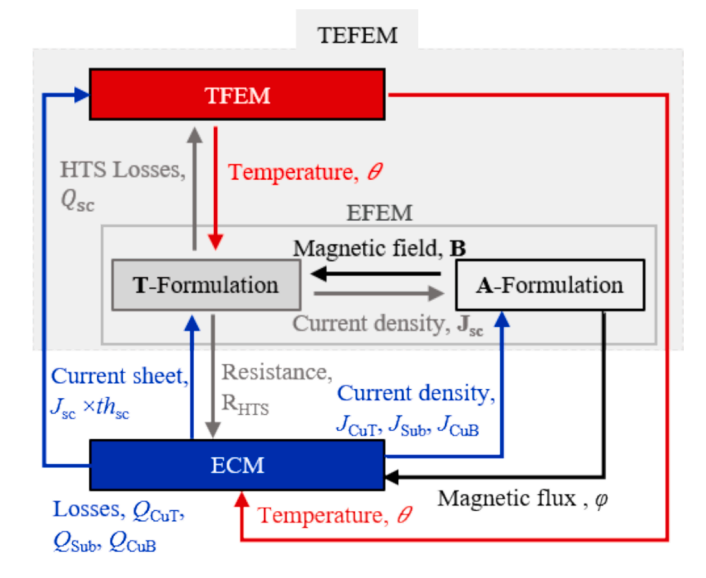


Fig. 6. Full model (TEFEM - ECM) for overcurrent simulations of inductive HTS coils. It is composed of three interacting submodels: 1) the electromagnetic FE model or EFEM (T-A formation), 2) the thermal FE model or TFEM, and 3) the electrical circuit model or ECM.

current density J_{sc} . The latter is derived from the current vector potential T as $J_{sc} = \nabla \times T$. The non-linearity of the resistivity of the superconductor to compute the actual distribution of the current density within the HTS layer.

The current vector potential T is solved in the Partial Differential Equation (PDE) module of COMSOL assuming that the superconductor is a 1D line [28]. Local variables, such as the nonlinear resistivity of the superconductor and the metallic layers are defined in the electromagnetic FE model and subsequently use to compute global variables, e.g. the resistances of the different layers to be used in the Electrical Circuit Model (ECM). Those variables are described in details in the Table 2 of Section 5. Besides the superconductor, the electromagnetic contributions of the Cu stabilizer ("Cu"), through its top ("CuT") and bottom ("CuB") layers, and the substrate ("Sub") are taken into account during the transition of the superconductor to its normal resistive state. These conductive layers are given as current density sources J_{CuT} , J_{CuB} and J_{Sub} in the A formulation. These current densities are derived from the ECM. Indeed, with the circuit model and the knowledge of the cross-section of each metallic layer, the current density flowing through a layer is computed from its current assuming a uniform distribution of the current density across the layer. The second submodel (TFEM) solves the heat balance equation using the heat transfer module of COMSOL. The heat sources are computed from the respective Joule losses in the superconductor, in the top and bottom Cu layers and in the substrate. The third and last submodel is the Electrical Circuit Model (ECM) which is worked out via the ordinary differential equation (ODE) module of COMSOL. This model provides the resistances of the different layers which are used to estimate the redistribution of current. For all the submodels, the domains are the superconductor, the top and bottom Cu layers and the substrate. The contribution of the silver layer is neglected compared to the contribution of the Cu layers. Indeed, its thickness is very small in comparison to the Cu thickness, $th_{Cu} \gg th_{Ag}$. Fig. 7 shows a schematic drawing of one turn of the coil (not to scale) with its turn-toturn insulation and the wound HTS tape as well as the simplified geometry used in the TEFEM - ECM. The submodels are detailed in the subsequent subsections.

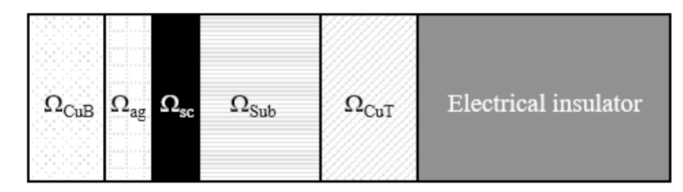
4.2. Electromagnetic finite element model (EFEM)

The problem is axisymmetric as shown in Fig. 8. The full T-A formulation of the Maxwell equations is used here. It is practical as the coil is only made of 6 turns. For such a formulation, the superconducting layers are considered as 1D lines [14]. The radial component of the current vector potential \mathbf{T} is solved over each line knowing the temporal variation of the magnetic flux density perpendicular to the line in the cylindrical coordinate system defined by (r, z). The equation for \mathbf{T} reads,

$$\frac{d}{dz}\left(\rho_{HTS}\frac{dT_r}{dt}\right) = -\frac{dB_r}{dt} \tag{2}$$

with $\rho_{\rm HTS}$ the resistivity of the superconductor. The radial component of the magnetic flux density B_r is given by $B_r = -dA_{\rm op}/dr$. The azimuthal

(a) One turn of the coil with its insulation and the HTS tape



(b) Geometric model used in the TFEM and the EFEM

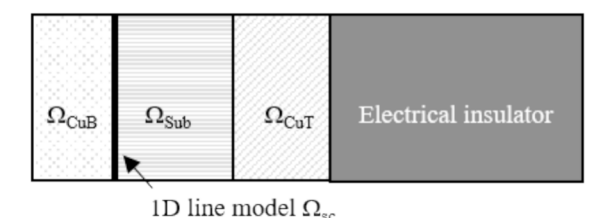


Fig. 7. (a) drawing (not to scale) showing one turn of the coil with its turn-to-turn insulation and the wound HTS tape; (b) shows the geometric model used in the TEFEM — FCM.

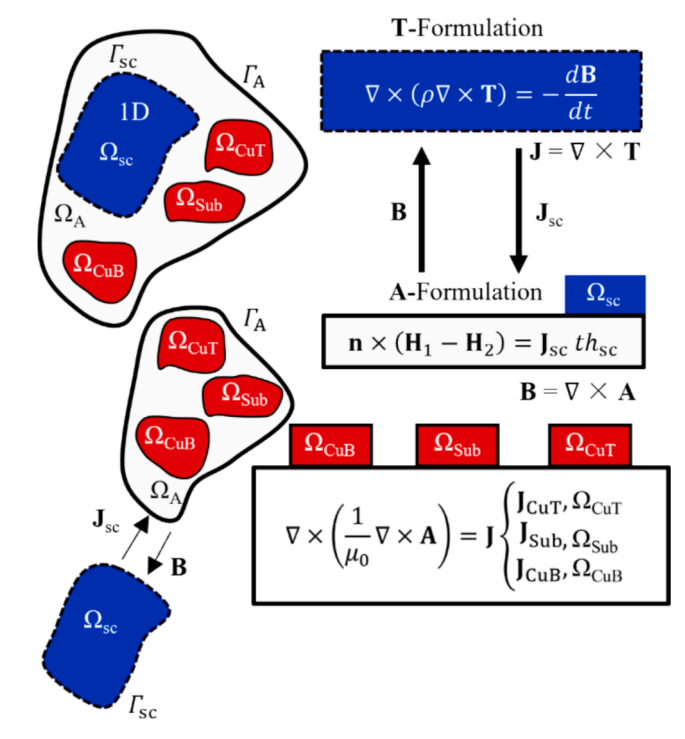


Fig. 8. Diagram showing the coupling between the two formulations T and A.

Table 2Expression of the electrical parameters such as resistance and inductive voltage for the three models; LBM, TBM and CBM presented in Fig. 12.

Parameters		Model	<u> </u>	<u>*</u>
		LBM	TBM	CBM
Resistance	HTS	$R_{sc,j} = \frac{2\pi r_{sc,j}}{w \cdot th_{sc}} \langle \rho_{sc}(J_j, \mathbf{B}_j, \theta_j) \rangle_w$		$R_{sc} = \sum_{j=1}^{N} \frac{2\pi r_{sc,j}}{w \cdot th_{sc}} \langle \rho_{sc}(J_j, B_j, \theta_j) \rangle_{w}$
	Metallic layer "i"	$R_{i,j} = \frac{2\pi \langle r_{i,j} \rangle}{w \cdot th_i} \rho_j (T_j)^*$		$R_{i} = \sum_{j=1}^{N} \frac{2\pi \langle r_{i,j} \rangle}{w \cdot th_{i}} \rho_{j} (T_{j})^{*}$
Inductive voltage	HTS	$U_{L,sc,j} = 2\pi r_{sc,j} rac{d\langle A_j angle_w}{dt}$	$U_{L,j} = 2\pi \frac{d \langle r_i A_j \rangle_{th,w}}{dt}$	$U_L = \sum olimits_{i=1}^N 2\pi rac{d\langle r_i A_j angle_{th,w}}{dt}$
	Metallic layer "i"	$U_{L,i,j} = 2\pi rac{d \langle r_{i,j} A_{i,j} angle_{th,w}}{dt}$	u	
• •	ly varies with temperature ductor ("CuT", "CuB" and "Sub")	ш		j index of the coil turnN number of turns of the coil

component of the magnetic vector potential A_{α} is obtained by solving,

$$\frac{d^2A_{\varphi}}{dr^2} + \frac{1}{r}\frac{dA_{\varphi}}{dr} - \frac{A_{\varphi}}{r} + \frac{d^2A_{\varphi}}{dz^2} = -\mu_0 J \tag{3}$$

where J is equal to $J_{\text{CuT}} = I_{\text{CuT}} / S_{\text{CuT}}$ and $J_{\text{CuB}} = I_{\text{CuB}} / S_{\text{CuB}}$ in the Cu domains Ω_{CuT} and Ω_{CuB} and is equal to $J_{\text{Sub}} = I_{\text{Sub}} / S_{\text{Sub}}$ in the substrate domain Ω_{Sub} . S is the cross section of each domain. The currents I_{CuT} , I_{CuB} , and I_{Sub} are obtained from the ECM whose coupling is introduced in subsection 4.4. The corresponding equations are further detailed in section 5. The current I_{Sc} in the REBCO is imposed as a boundary Dirichlet condition on the radial component T_{r} of the current vector potential T [14].

The resistivity ρ_{HTS} in (2) includes the two regimes for which there is still current in the superconductor, i.e., when the superconductor is in its superconducting state ($I_{sc} < I_c$ and $\theta < \theta_c$), and when the superconductor is in its current sharing regime ($I_{sc} \ge I_c$ and $\theta < \theta_c$). To smoothen the transition between the two regimes, the resistivity of the superconductor is combined with its normal-state resistivity such that,

$$\rho_{HTS}(\theta, \mathbf{B}, J_{sc}) = \frac{\rho_{sc}(\theta, \mathbf{B}, J_{sc}) \cdot \rho_{nsc}(\theta)}{\rho_{sc}(\theta, \mathbf{B}, J_{sc}) + \rho_{nsc}(\theta)}$$
(4)

where $\rho_{\rm SC}$ is the resistivity of the superconductor in its superconducting state and $\rho_{\rm nSC}$ is the resistivity of the superconductor in its normal-resistive state. θ is the temperature of the superconductor.

On the other hand, in the normal-state regime, the resistivity of the superconductor takes the simpler expression (5).

$$\rho_{HTS}(\theta) = \rho_{nsc}(\theta) \tag{5}$$

here, the resistivity $\rho_{\rm nsc}$ is given by,

$$\rho_{\rm nsc}(\theta) = \rho_{\rm nsc,\theta} \cdot \theta + \rho_{\rm nsc,c} \tag{6}$$

where the following choices were made: $\rho_{nsc,\theta}=12.5\times 10^{-8}~\Omega$ m K $^{-1}$ and $\rho_{nsc,c}=2.22\times 10^{-11}~\Omega$ m [29].

The resistivity $\rho_{\rm sc}$ is inferred from the power law (1) such that,

$$\rho_{sc}(J_{sc}) = \frac{E_c}{J_c^n} J_{sc}^{n-1} \tag{7}$$

It is assumed that $J_{\rm sc}=I_{\rm sc}/S_{\rm sc}$, where $S_{\rm sc}$ is the cross section of the superconducting layer and $I_{\rm sc}$ is its current. The critical current density $J_{\rm c}$ is given by the Kim relation [30],

$$J_{c}(\theta, \mathbf{B}) = \frac{J_{c,\theta}(\theta)}{\left(1 + \frac{\sqrt{k_{f}^{2}B_{//}^{2} + B_{\perp}^{2}}}{B_{0}}\right)^{\beta}}$$
(8)

where $B_{//}$ and $B\perp$ are the parallel and perpendicular components of the magnetic field compared to the tape surface. k_f , β , and B_0 are the shape parameters representing the anisotropy characteristics of textured thin REBCO strips. For this study, these parameters are: $k_f=0.1115$, $\beta=1.7825$, and $B_0=253.5$ mT [31]. The temperature dependency of J_c is given by [32],

$$J_{c,\theta}(\theta) = \left(\frac{\theta_c - \theta}{\theta_c - \theta_0}\right) \cdot J_{c,0} \tag{9}$$

 $\theta_{\rm c}$ is the critical temperature of the superconductor, and θ_0 is the temperature of the liquid nitrogen equal to 77 K. This value is taken as the reference temperature for determining $J_{\rm c0}$. The latter is the self-field critical current density given by $J_{\rm c0} = I_{\rm c0} / A_{\rm sc}$, and equal to 8.9286 \times 10⁹ A m⁻².

4.3. Thermal finite element model (TFEM)

The TFEM is also axisymmetric. Hence, each turn "j" of the coil

exchanges heat radially and vertically with their surroundings. Moreover, it is assumed that there is no heat diffusion along the tape length and that its properties are homogeneous and isotropic. The distribution of temperatures θ in the superconductor, the top Cu layer, the bottom Cu layer and the substrate is solved via the Heat Transfer module of COMSOL under given boundary and initial conditions. In the present work, there is little incentive to use a lumped-parameter model to interact with the FEM as the accuracy would decrease for a gain in computation time that would not justify the loss, especially in the inductive case as discussed in [33]. It is shown in the next section 5 that the substantial gain is mostly determined here by reducing the model of the electric circuit. Nevertheless, this is undoubtedly an improvement that can be done to the present TEFEM-ECM down the road; particularly to address the simulation of large systems more demanding in terms of computational resources.

The governing heat balance equation is recalled below,

$$\gamma C_p \frac{d\theta}{dt} + \nabla \cdot (-k\nabla \theta) = q \tag{10}$$

where γ is the mass density (kg m⁻³), C_p is the specific heat capacity (J kg⁻¹ K⁻¹), k is the thermal conductivity (W m⁻¹ K⁻¹) and q the Joule dissipation (W m⁻³). The initial condition assumes that all the system is at the temperature of LN2 (77 K). Geometric details of the thermal model and the corresponding boundary conditions are shown in Fig. 9. On the surfaces in contact with the coil support, the heat flux is set to zero (dashed red lines). On the surfaces in contact with liquid nitrogen, the heat flux (W m⁻²) is given by the convective heat flux q_0 (dashed blue lines). The specific heat capacities and thermal conductivities are temperature-dependent as for the electrical resistivities [34].

The volumetric dissipation q takes place in the conductive layers of the tape, i.e., the superconductor and the metallic layers (top and bottom Cu layers and substrate) so that $q_j = q_{sc,j} + \sum_i q_{ij}$, with "i" the index corresponding to "CuT", "CuB" and "Sub". It is recalled that the thermal and electrical impact of the silver layer is neglected in the present model. In addition, since the superconducting layer is modelled as a 1D line, its Joule loss in W m $^{-3}$ given by $q_{sc,j} = \rho_{sc,j} \times J_{sc,j}^2$ over the turn "j" is transformed into a surface heat loss in W m $^{-2}$ as $q_{sc,j} \times th_{sc}$, with th_{sc} the thickness of REBCO. It is therefore treated independently of the volumetric losses in the metallic layers. So, instead of being imposed as a volumetric heat source, it is given as a boundary source over the 1D line in the TFEM. The remaining metallic layers dissipate $q_{i,j} = R_{i,j} \times I_{i,j}^2 / V_{i,j}$, with $V_{i,j} = 2\pi r_{i,j} \times A_i$ the volume of the conductor layer "i" over the

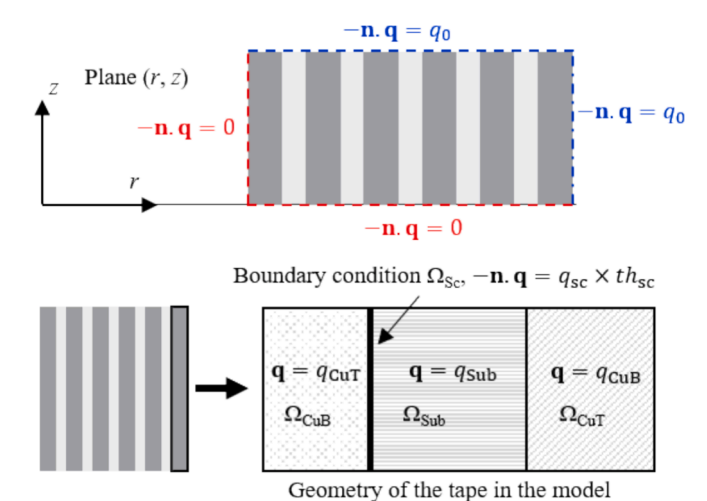


Fig. 9. Boundary conditions in the thermal model. Dashed red lines: zero heat flux, dashed blue lines: convective heat flux q_0 . (For interpretation of the references to colour in this figure legend, the reader is referred to the web version of this article.)

turn "i" of the coil at radius $r_{i,i}$.

The convective heat flux q_0 is difficult to assess. It is typically obtained in near ideal cases where the shape of the sample, the state of the surface, and the positioning of the sample in the bath (vertical, horizontal or in between) are defined. It is not clear how to translate this bulk of knowledge into the specificities of the present case study involving a coil. Hence, in the present case, various existing heat transfer curves obtained from literature have been utilized to cover the possible thermal conditions experienced by the coil. Making an educated guess, it is expected that the proper heat exchange for the present experimental conditions is found amongst the combined curves. These heat transfer curves, compiled in Fig. 10, were obtained from the literature for a nitrogen bath at 77 K in steady state assuming that the temperature of the liquid was constant [35-39]. Besides 77 K, measurements of convection heat flux in subcooled liquid nitrogen can be found at operating temperatures of 65 K and 70 K [40,41]. These measurements can then be used for modeling superconducting coils at other conditions than a liquid nitrogen bath at 77 K with natural convection.

From the data collected in [35–39], a surface encompassing any possible heat transfer curves, referred to as the operating envelope, has been built and shown. Its lower and upper limits, $q_{0 \min}$ and $q_{0 \max}$, are considered the weakest and the strongest convective heat fluxes available at the interface of the coil in contact with the LN2. This hypothesis is checked in section 6 where a comparison between simulation results and measurements is presented for the two curves $q_{0 \min}$ and $q_{0 \max}$.

4.4. TEFEM - ECM coupling

For overcurrent applications, the purpose of coupling the ECM and the TEFEM is to determine the current distribution between the parallel-connected layers of the tape during the different stages of the transition between the superconducting and the normal-resistive states, i.e. from the onset of the current sharing regime to the quench of the superconductor, as presented in subsection 4.1. As mentioned previously, the presence of the silver is neglected. The current distribution computed in the ECM is then defined by the ratio of the respective resistances of the superconductor, the Cu layers and the substrate. It should be noted that, in the case of a quench, the superconductor, having a large resistance, is no longer considered and the current flows solely in the metallic layers.

The ECM makes use of global variables (currents and voltages) combined with lumped parameters (resistances), whereas the TEFEM

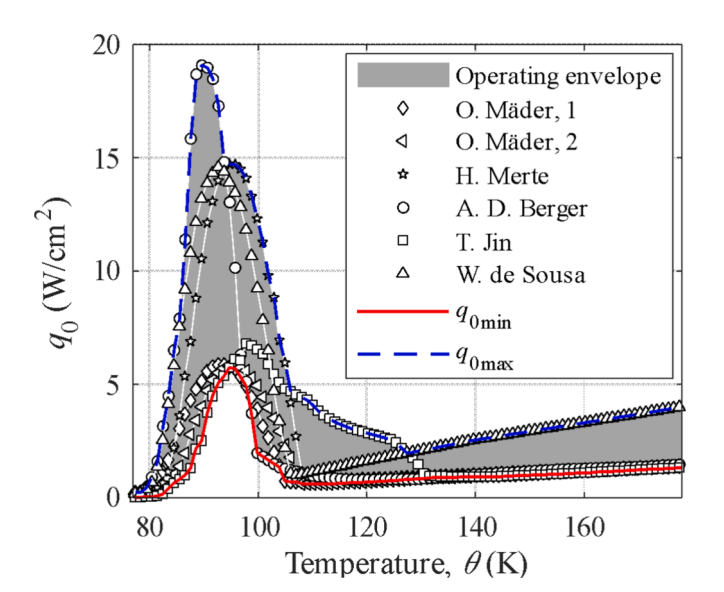


Fig. 10. Review of heat fluxes measured between solid and liquid nitrogen at 77 K: O. Mäder, 1 [34], O. Mäder, 2 [34], H. Merte [35], A.D. Berger [36], T. Jin [37], W. de Sousa [38].

computes local variables such as the magnetic vector potential and the temperature. These local variables are necessary to calculate the global variables and the lumped parameters. Thus, the magnetic vector potential ${\bf A}$ is integrated to yield the voltage; the temperature θ is used to estimate the resistivities in each domain which are then used to estimate the electrical resistances. These resistances determine the distribution of current in the tape, effectively coupling both submodels. Fig. 11 shows the flux of exchanged variables, global and local, between the TEFEM and the FCM

For the circuit model, the governing equations follow Kirchhoff's laws of voltage and current. For a single turn "j" of the coil, the voltage reads,

$$U_j = U_{R,j} + U_{L,j} \tag{11}$$

where U_j is the turn voltage summing the resistive voltage $U_{R,j}=R_j\times I_j$ and the inductive voltage $U_{L,j}$. Here, the equivalent resistance R_j is derived from the resistances of the different layers knowing their temperature-dependent resistivities as $R_j=R_{i,j}$ // $R_{sc,j}$ with $R_{i,j}$ the parallel resistances of the metallic layers "i" in the turn "j" and $R_{sc,j}$ the resistance of the superconductor in the turn "j". The inductive voltage is computed from the local time variation of the magnetic vector potential. The inductive voltage is naturally represented by the opposite electromotive force + d φ /dt assuming that each turn is an independent loop of current carrying the same current I supplied by the discharge system. The relation between the turn voltage U_j and the voltage along the different layers is given according to the parallel circuit model as,

$$U_{j} = U_{CuT,j} = U_{sc,j} = U_{j} = U_{CuB,j}$$
 (12)

The coil voltage U_{coil} of the entire coil is then inferred from the sum of the turn voltages, and,

$$U_{coil} = \sum_{i=1}^{N} U_i \tag{13}$$

with *N* the number of turns in the coil.

In the same parallel circuit model, the Kirchhoff's law of current yields the following relation,

$$I = I_{CuTj} + I_{scj} + I_j + I_{CuBj}$$

$$\tag{14}$$

where I is the pulsed current generated during the discharge of the capacitor C into the circuit (see Fig. 5). For consistency with the TEFEM, only the superconducting layer, the top and bottom Cu layers and the substrate were considered in the ECM resulting in four parallel-connected resistances in series with an electromotive force. However, in the reduced ECM, instead of being defined on a turn-by-turn basis, the parallel resistances and the electromotive force are averaged over the whole coil. This reduction of the ECM is introduced and validated in the next section 5. In the same section, the equations relating the local variables obtained from the TEFEM and the global variables and the lumped parameter passed to the ECM are detailed.

5. Reduction of the electrical circuit model

In this section, a reduction of the ECM is introduced. Specifically, a simplification of the ECM is proposed by replacing the use of self and mutual inductions with a more concise representation based on inductive voltage (electromotive force). To validate this reduced electrical circuit model, a step-by-step methodology is taken below. It considers three different ECM of decreasing complexity. These ECM are presented in Fig. 12. Each ECM corresponds to a step in the model reduction. The corresponding global variables and lumped parameters are presented in Table 2. It provides the equations relating the local variables such as the magnetic vector potential $\bf A$, the current density $\bf J$, and the temperature θ , computed in the TEFEM to the resistances (lumped parameter) and the coil voltage U_{coil} (global variable) in the ECM.

The first ECM is given in Fig. 12(a). It is the most accurate

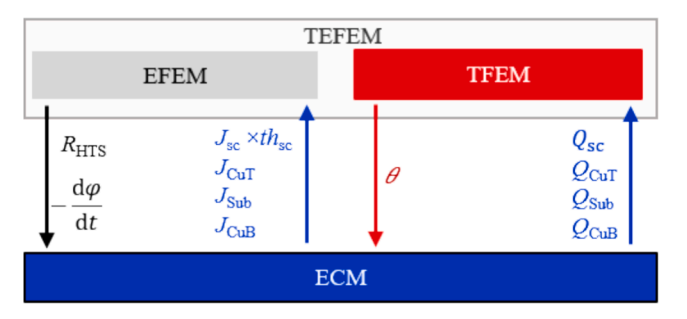


Fig. 11. Exchange of variables between the ECM and the TEFEM. The latter is composed of the electromagnetic model (EFEM) coupled to the thermal model (TFEM).

representation of the actual electrical behavior of the coil. It is referred to as the layer-based model or LBM as each layer holds a layer resistance in series with a layer electromotive force. This model is subsequently simplified by moving out the electromotive forces of each layer to build a single turn-based electromotive force, see Fig. 12(b). This electromotive force on a turn basis represents the induction of one turn of the coil. The parallel resistances are computed on a turn basis as well but distinguishing each individual layer in the turn. This model is referred to as turn-based model or TBM. Finally, the turn-based electromotive forces and the turn-based parallel resistances are lumped into a single set of equivalent parallel resistances in series with one electromotive force as illustrated in Fig. 12(c). This ultimate reduction is done by averaging the magnetic vector potential and the temperature over the coil. This last model is subsequently referred to as coil-based model or CBM. It is worth noting that moving from the layer-based electromotive force of Fig. 12 (a) to a single turn-based electromotive force of Fig. 12(b) is already a significant simplification of the ECM. Indeed, as the current redistributes between layers, each layer ought to be included. So, in addition to its resistance, its own electromotive force combining the time variation of the self and mutual magnetic fluxes should be added to provide a seemingly impedance per layer. This difficulty has been lifted here by reducing the electrical model where the lumped resistance of each layer in the turn "j" is the driver of the Joule dissipation for the heat balance equation, whereas the turn induction associated with the magnetic flux produced by the turn itself and its mutual magnetic flux shared with the other turns is lumped into a single electromotive force for the entire coil.

As a complimentary note on the inductance model, if the current density is uniform in the tape, the inductive voltage depends solely on the geometry of the coil and can be represented in first approximation by an inductance times the rate of change of the current, or $U_L = L \, dI \, / dt$. This inductance can be determined by magnetostatics calculations from the magnetic energy [42]. In the case of a HTS tape, the distribution and the path of the current density changes according to the magnetic shielding of the superconductor subjected to varying magnetic flux as well as during the redistribution of current between the layers of the tape in the current sharing regime. In both cases, the current density is non-uniform and the inductance representation would become improper.

To check at once all those various assumptions, a direct validation is carried out via simulation using a unique TEFEM coupled to the three different ECM. Thus, the coil is simulated under overcurrent conditions as described in section 3. Table 3 provides the relation between the peak capacitor voltage $U_{\rm c0}$ and the ratio $I_{\rm max}/I_{\rm c}$. For all the three ECM, the maximum thermal heat flux curve $q_{\rm 0max}$ given in Fig. 10 has been utilized. For those runs, the same mesh was used consisting of 12,881 nodes and 25,710 simplexes. The number of degrees of freedom (DOF) of the full TEFEM – ECM was 71,243 considering the LBM, 57,536 for the TBM and 57,516 for the CBM. The computer is equipped with an Intel® Xeon® E5-2630 v4 processor, using 2 sockets of 10 cores each.

Fig. 13 shows a comparison of the coil current I_{coil} between the three

ECM coupled to the same TEFEM. The coil current is the pulsed current flowing through the coil. The corresponding coefficient of determination R^2 or Pearson correlation coefficient, see [43] for a general expression, taken the LBM as reference, is shown in Table 4. A value above 0.99 was found for all cases indicating a very good likeness between the results. Fig. 14 shows the coil voltage for different discharges with its corresponding R^2 given in Table 4. Here too, a good agreement is achieved with a R^2 larger than 0.99.

Fig. 15 provides the computation time of the TEFEM - ECM for the three ECM. There is a large gain moving from the LBM to the CBM. This order of magnitude difference is not explainable by the mere increase of 20 % in the DOF between the TBM (or CBM) and the LBM. The more likely explanation can be found in the slow convergence originating from the strong non-linearity of the model in the current sharing regime. In this regime, a smaller time step is required to compute the current density distribution in the superconductor catching as well the redistribution of current in the different layers of the tape. This is stressed out in the LBM where all the turns of the coil are simulated with all the layers of each tape being considered. However, in the CBM, a single equivalent model is used to represent the entire coil reducing drastically the number of computation to be carried out (see Fig. 12). Passing the current sharing regime, the model is essentially linear as all the current flows in the metallic layers alleviating the number of iteration for the Newton-Rapshon and allowing the solver to increase the time step. Overall, the TBM and CBM present the same order of magnitude in terms of computation speed with the CBM having the speediest computation. Interestingly, around $I_{\text{max}}/I_{\text{c}} = 4$, all the models saw a bump in their computation time due to a slower convergence of the nonlinear system. There, the automatic time step lowers to catch the quench dynamic as the problem becomes stiffer. Finally, whereas the computation time for the LBM ranges from less than an hour to more than 20 h, the TBM and CBM do not go over 4 h (TBM) with the CBM remaining under 2 h for a complete simulation time equal to 35 ms.

Having demonstrated the relevance of the model reduction yielding a fair accuracy at a reduced computation time, the CBM was then used to validate the TEFEM — ECM in the next section 6.

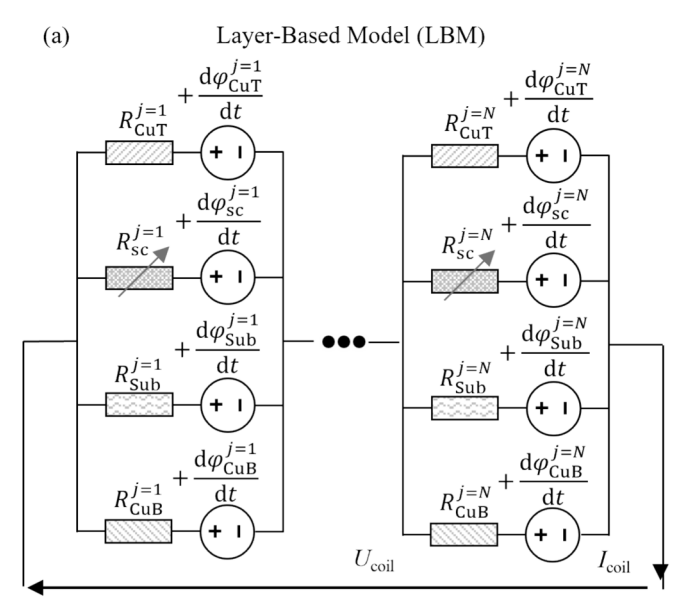
6. Comparison of simulation results with experimental data

The results of the proposed TEFEM — ECM, using the reduced CBM as presented in Fig. 12(c), is compared to experimental data for overcurrent conditions. Here, the inductive HTS coil is subjected to different pulses of increasing current amplitudes given by the peak capacitor voltage $U_{\rm c0}$. The relation between $U_{\rm c0}$ and the ratio $I_{\rm max}/I_{\rm c}$ is given in Table 3. It is recalled that the peak pulsed current $I_{\rm max}$ ranges from the critical current of the coil $I_{\rm c}$ to $5.6 \times I_{\rm c}$. After each pulse, a period of 30 s is observed to allow the tape to recover its initial temperature equal to

Out of 12 runs of overcurrent tests, we present here only five of them to stress out the different regimes of the superconductor. These regimes are the current sharing and the full transition to the normal-resistive state. Most of the remaining runs were conducted in the full transition regime duplicating the latter results without bringing any relevant additional information. Nonetheless, all the simulation results were processed and analysed for all of the 12 experimental runs and compared to experimental data via the coefficient of determination (R^2) .

6.1. Global variables: Pulsed current and coil voltage

Fig. 16 shows a comparison between the experimental measurements and the simulated data of the coil current as a function of time for various magnitudes of the peak capacitor voltage U_{c0} ranging from 250 V to 700 V. A very good agreement is achieved on the evolution of the coil currents over the course of the tests. Indeed, as shown by Fig. 17, the coefficient of determination R^2 varies between 0.9988 and 1 for each individual peak of coil current I_{max} independently of the choice of the



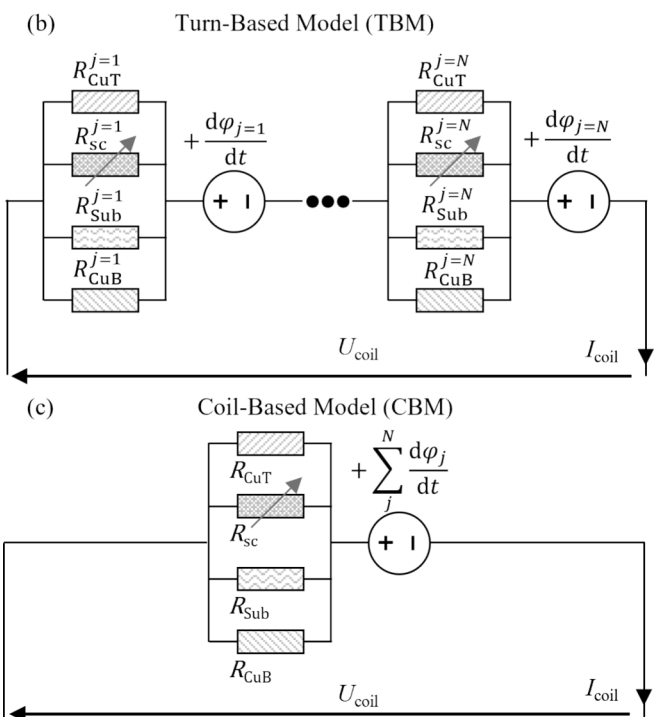


Fig. 12. (a) provides the most accurate ECM of the inductive coil in transient (layer-based model or LBM); (b) shows the intermediate model (turn-based model or TBM) leading to the reduction of the ECM given in (c) (coil-based model or CBM).

Table 3 Values of $I_{\rm max}/I_{\rm c}$ according to the peak capacitor voltage $U_{\rm c0}$.

<i>U</i> _{c0} (V)	250	350	450	600	700
$I_{\rm max}$ $/I_{\rm c}$	1.87	2.64	3.42	4.89	5.62

heat transfer curves indicating a very good likeness between results. For the calculation of R^2 , the reference values are given by the experimental measurements. It is recalled that the maximum and minimum heat transfer curves, $q_{0 \min}$ and $q_{0 \max}$, are the maximum and minimum curves enveloping the different heat transfer curves found in the literature (operating envelope) and compiled in Fig. 10.

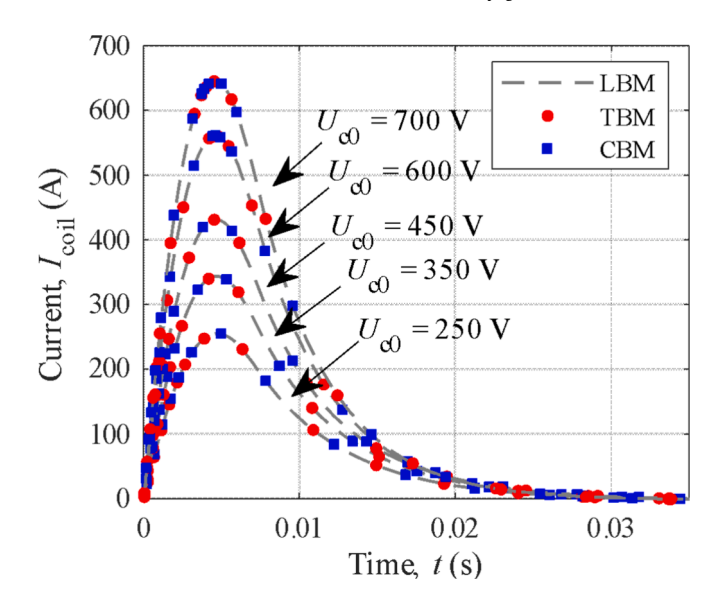


Fig. 13. HTS pulsed current flowing through the HTS coil or coil current I_{coil} versus time for different values of the peak capacitor voltage U_{co} (Fig. 5).

Fig. 18 shows the experimental coil voltages and the simulated ones corresponding to the coil currents given in Fig. 16. The grey coloured area represents the envelope corresponding to the simulations carried out with the minimum and maximum heat transfer curves, q_{0min} and $q_{0\text{max}}$. It can be observed that the TEFEM – ECM predicts fairly well the evolution of the coil voltage. Indeed, the envelope encompasses the actual experimental measurements. The largest incertitude (wider red area) is found for a peak capacitor voltage U_{c0} equal to 350 V and 450 V for which the coil current is not large enough to lead to a thermal runaway but still showing a significant temperature rise ($\theta > 85$ K, see Fig. 20). In this overcurrent test, the temperature reaches a maximum value before decreasing as the current supplying the Joule losses vanishes within 30 ms. There is not enough time to lead to an uncontrollable temperature rise since the current decreases fast enough to cut off the thermal runaway in its path. For the extreme heat transfer curves, the R^2 , presented in Fig. 19, drops from more than 0.9, indicating a good overall likeness between simulated and experimental curves, to less than 0.8, indicating a significant deviation from experimental data. However, this deviation is localised in time. It occurs during the recovery of the coil for a situation where the coil does not experience any thermal runaway throughout the test.

The temperature evolutions given in Figs. 20 and 21 are not measured but estimated from the coil voltages. Thus, knowing the theoretical inductance of the coil L and consequently the inductive voltage $U_L = L \, dI \, / dt$, the resistive voltage U_R of the coil can be extracted from the total coil voltage $U_{\rm coil}$ according to (15). Here, the inductance representation is used as the current density is assumed uniform. The inductance is derived from the magnetic energy computed in magnetostatics on the basis of the previous assumption.

$$U_R = U_{coil} - L \frac{dI}{dt} \tag{15}$$

From the resistive voltage U_R , the combined resistance of the metal layers in the tape, averaged over the coil, can be estimated using Ohm's law as $R_m = U_R / I$, where I represents the coil current (equivalent to the pulsed current). Furthermore, the average resistivity ρ_m of the tape used in the coil has been measured through conduction cooling within an operating range of 100 K to 300 K. It can be expressed as a function of temperature in the form of:

$$\rho_m(\theta) = 10^{-9} \times (0.1713 \cdot \theta[K] - 6.8849)$$
 (16)

With this information, it is possible to estimate the temperature of

Table 4Comparison of TEFEM – ECM coupling for three configurations: LBM, TBM, and CBM.

Model	DOF	R ² of current	R ² of voltage	Average computation time $T_{\rm q}$
LBM	71,243	Reference Model	Reference Model	6.097 h
TBM	57,536	0.999998	0.9997832	1.396 h
CBM	57,516	0.9999971	0.9990667	0.904 h

^{*} are the average values derived from all the curves in Figs. 13, 14 and 15. R^2 is the Pearson correlation coefficient.

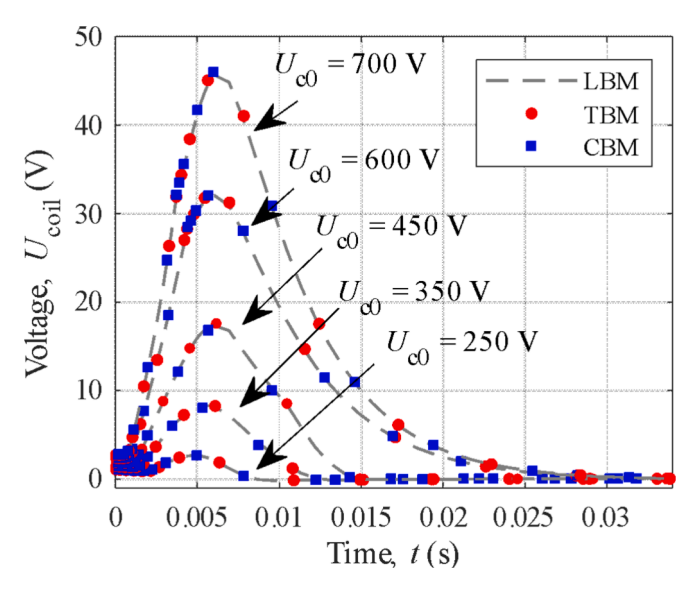


Fig. 14. HTS coil voltage as a function of time for different values of the capacitor voltage U_{c0} shown in Fig. 6.

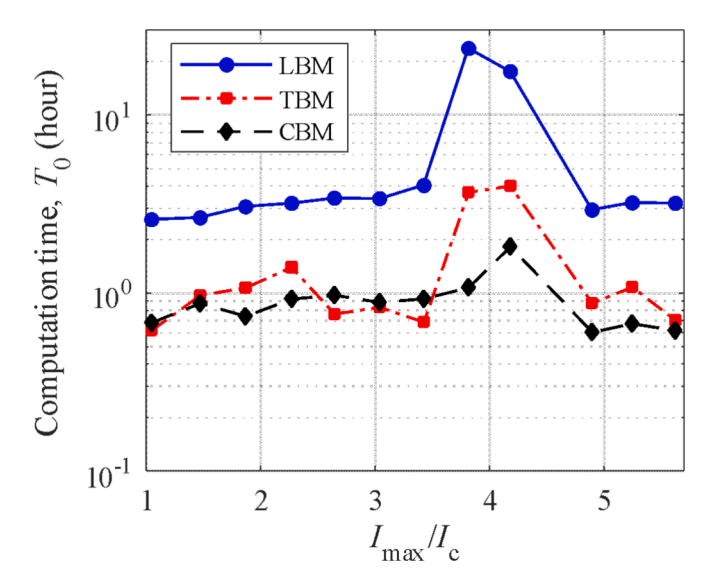


Fig. 15. Computation time for the different ECM. Overall, the fastest model (TEFEM - ECM) is the CBM.

the coil at the time of quenching by knowing the value of its average resistivity. This post-processing allows calculating an average temperature over the coil which is subsequently compared to the simulated temperature for the different cases corresponding to $U_{\rm c0} \geq 450$ V. It should be noted that when the tape remains fully or partially in its superconducting state ($U_{\rm c0} \leq 350$ V), no average temperature can be estimated, and the Figs. 20 and 21 provide only the simulated temperatures. In those specific cases, the temperature is expected to increase

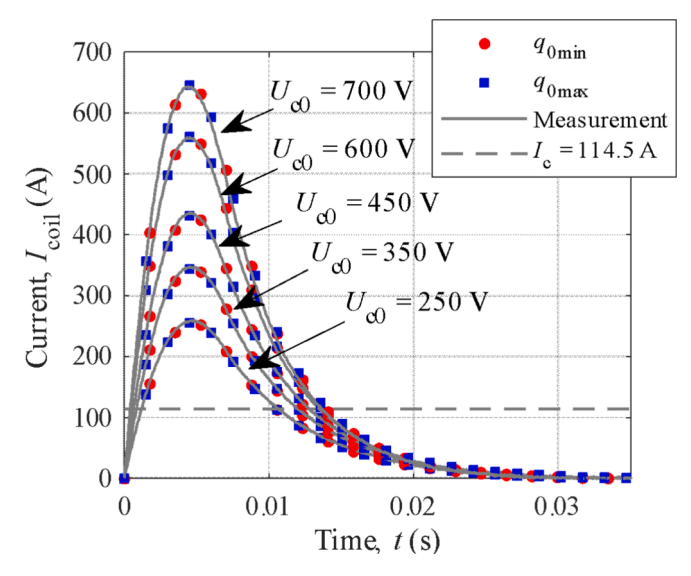


Fig. 16. Coil current versus time for different values of the peak capacitor voltage $U_{\rm c0}$.

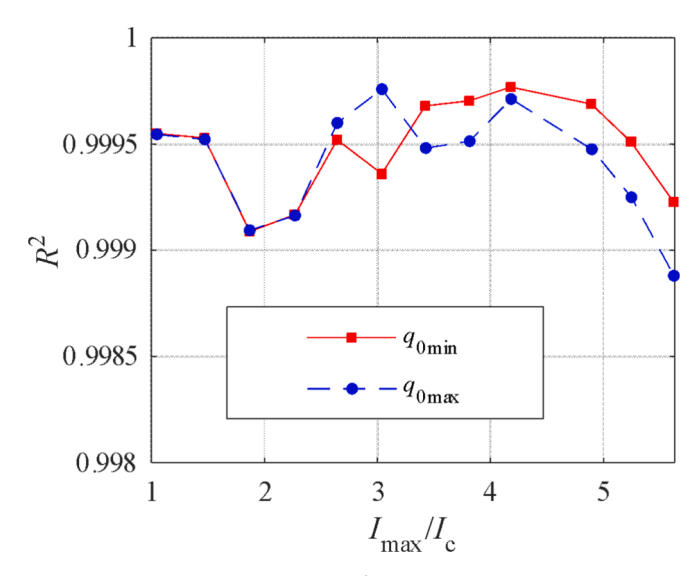


Fig. 17. Coefficient of determination (R^2) for all of the 12 runs comparing the current of the HTS coil calculated by the TEFEM - ECM to the corresponding experimental data as a function of $I_{\rm max}/I_{\rm c}$.

marginally and the simulated coil voltages fit the experimental results with the lowest dispersion arising from the choice of the heat transfer (thinner grey area). When the tape quenches ($U_{\rm c0}>450$ V), the coil voltage is fairly well simulated throughout the overcurrent tests with a moderate dispersion at peak coil current. The simulated temperatures, shown in Fig. 20, are found to overestimate the temperature peak post-processed from measurements at ratios $I_{\rm max}/I_{\rm c}$ larger than 4.5. The temperature evolutions for the simulations and experiments, given in

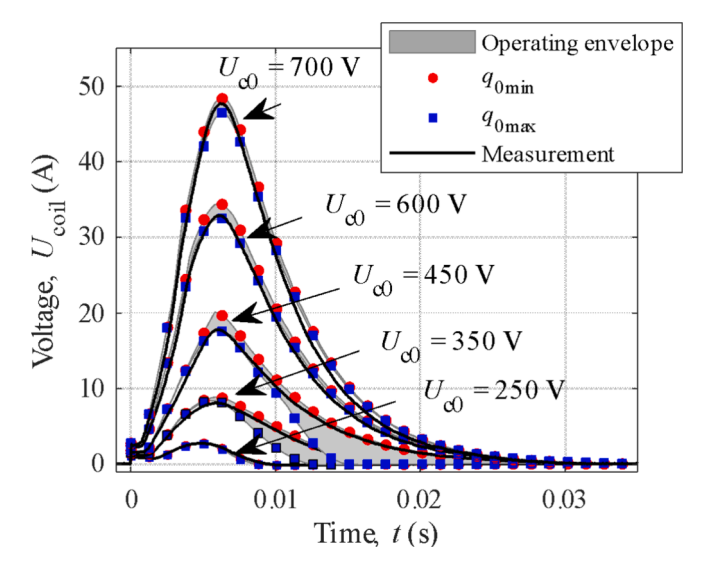


Fig. 18. Coil voltage as a function of time for different values of the capacitor voltage $U_{\rm c0}$.

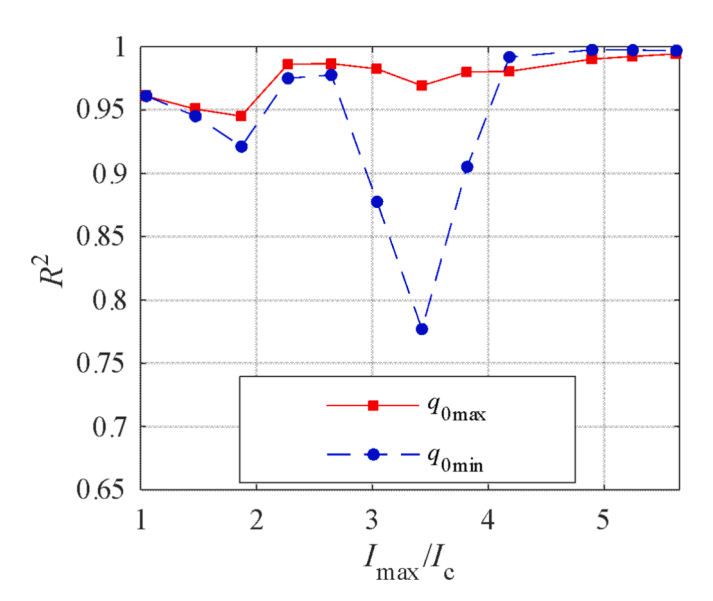


Fig. 19. Coefficient of determination (R^2) for all of the 12 runs comparing the voltage of the HTS coil calculated by the TEFEM - ECM to the corresponding experimental data as a function of $I_{\rm max}/I_{\rm c}$.

Fig. 21, show a reasonable agreement with the best accord obtained at the beginning of the quench between 0.004 s and 0.01 s before slightly diverging. The largest dispersion (the largest grey area), with a predominance in the recovery stage, is found in the current sharing regime touching barely the onset of a quench (350 V \leq $U_{c0} \leq$ 450 V). In this condition, the behaviour of the superconductor is still well approximated by the power law with a full dependency on temperature and magnetic flux density. The recovery stage is more complex to simulate as hysteresis effects can take place at the interface of the solid and the liquid nitrogen leading to a rather different heat transfer cooling in the recovery than in the onset of the quench [44]. It should be noted that the temperature obtained from measurements seem to diverge even though the peak pulsed current passed. This artefact results from the vanishing of the coil current at which point the post-processing breaks down.

Out of this analysis, it is clear that the initial educated guess on the likeliness of the actual heat transfer being in the range of available heat transfer curves from literature has been checked. Over the course of the overcurrent test for a given ratio $I_{\rm max}/I_{\rm c}$, the heat transfer model shifts

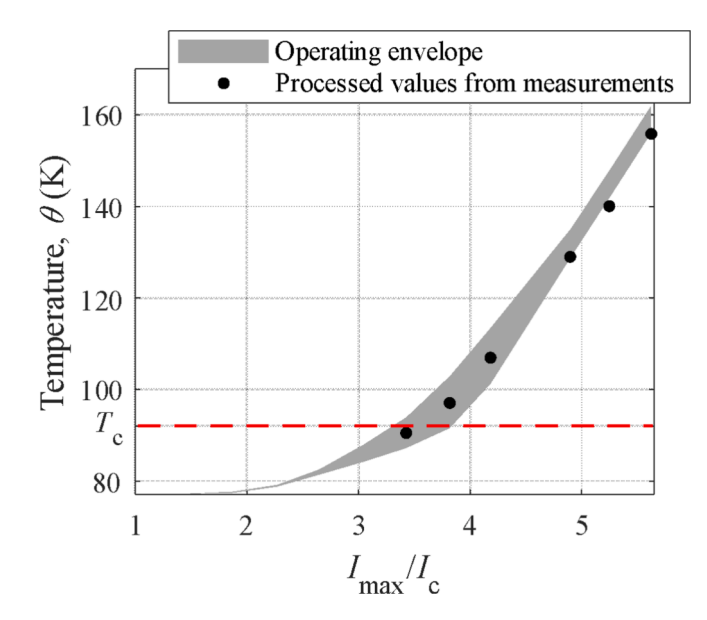


Fig. 20. Average temperature of the superconducting coil as a function of $I_{\rm max}/I_{\rm c}.$

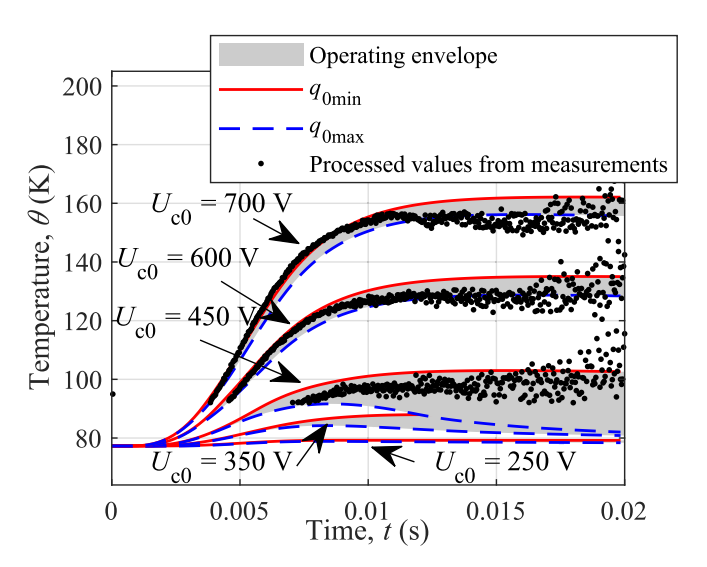


Fig. 21. Average temperature of the superconducting coil versus time for different discharge capacitor voltage values U_{c0} .

from the maximum heat transfer curve $q_{0\text{max}}$ to the minimum heat flux $q_{0\text{min}}$ as shown in Fig. 21, but it remains mostly in between as shown in Fig. 20, before a thermal runaway sets in and the temperature tends to diverge. This difficulty in defining clearly the heat transfer throughout the overcurrent test arises from the complexity to accurately simulate the detailed local thermal response of the coil to the presence of the liquid nitrogen. An empirical approach is then usually employed as no experimental data on different coil configurations and thermal conditions are available in the literature or easy to obtain experimentally.

6.2. Local variables: Magnetic flux density, normalized current density and temperature

Fig. 22 presents some local variables computed in the TEFEM at different times over the pulse duration for a peak capacitor discharge voltage equal to 450 V. At this voltage, the temperature is slightly above the critical temperature without leading to a thermal runaway at the interface between the current sharing regime and the full transition

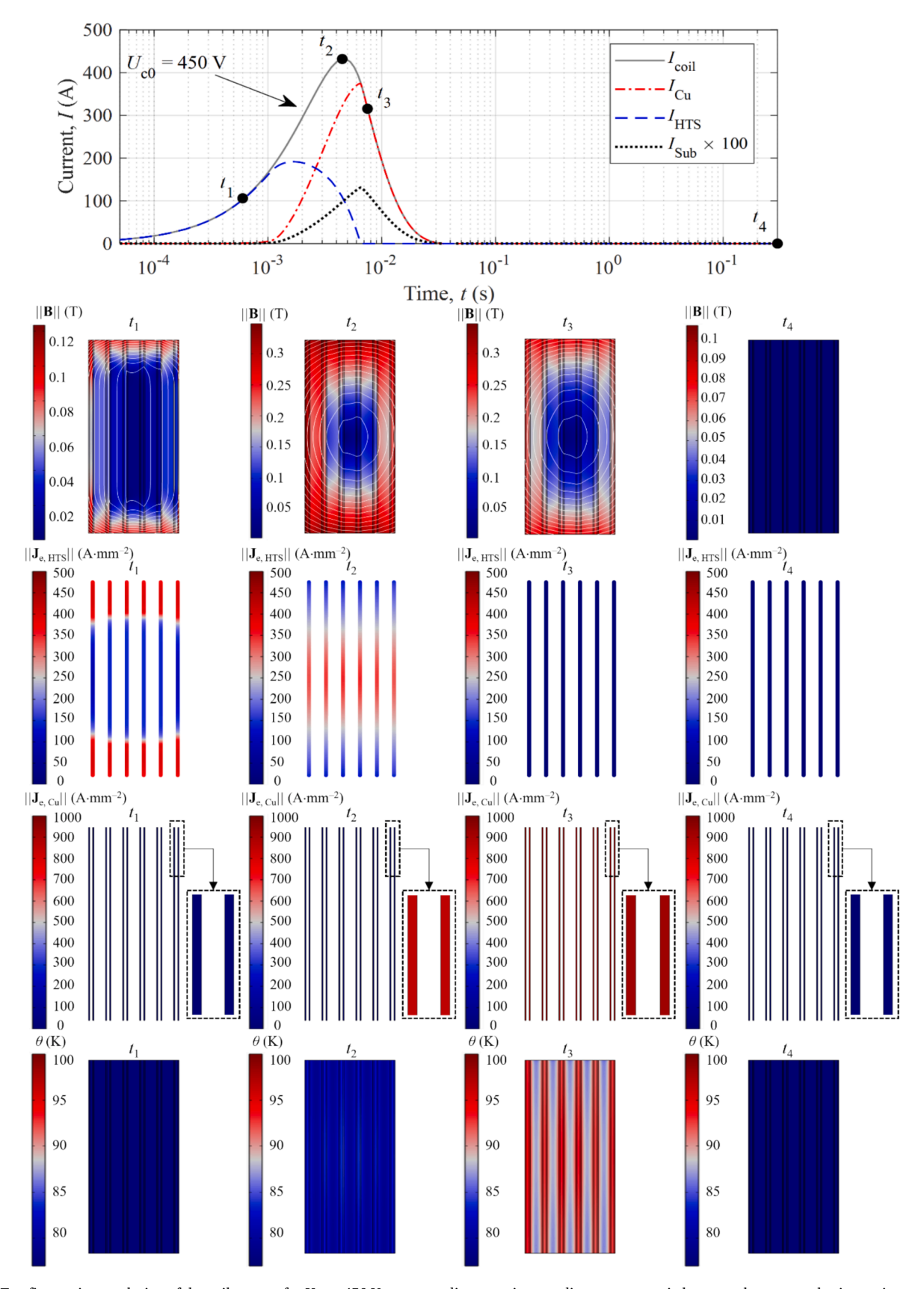


Fig. 22. Top figure, time evolution of the coil current for $U_{c0} = 450$ V corresponding to an intermediate case scenario between the current sharing regime and the full transition. Bottom figure, local variables of interest (B, J and θ) over the superconductor width at different times during the overcurrent test indicated in the top figure. J_{e, HTS} and J_{e, Cu} are the engineering current densities of the superconducting layer and copper, respectively.

according to Fig. 21.

The top Fig. 22 shows the redistribution of current in the different layers. As the resistance of the substrate is larger than the remaining metallic layers, it carries less current. Most of the current goes through the Cu layers as the current subsides in the superconductor due to the increase in temperature. At the end of the pulse, the current flows anew in the superconductor as the current and temperature are below their respective critical values. The local variables are the norm of the magnetic flux density over the coil cross section, the normalized current density in the superconducting layer, and its corresponding temperature. Four distinct times are probed: t_1 , t_2 , t_3 and t_4 . At $t_1 = 0.6\,$ ms, the coil current I_{coil} is slightly below the critical current I_c of the coil, with a ratio of $I(t_1)/I_c(77 \text{ K}) = 0.93$. The coil temperature is 77 K, and the current density distribution across the superconductor is non-uniform. This distribution approximately matches the magnetic field distribution. At $t_2 = 4.5$ ms, the current, being 3.72 times higher than the critical current, begins to leave the superconducting layer and start redistributing into the metallic layers of the tape. During this phase of current sharing, the coil temperature remains below the critical temperature θ_c of 92 K, thanks to thermal inertia. On the magnetic side, the flux density is generated by both the superconducting layer and the metallic layers. This is confirmed by the engineering current density norms in the superconducting layer and the copper layer ($||\mathbf{J}_{e, HTS}||$ and $||\mathbf{J}_{e, Cu}||$), which are 300 A mm⁻² and 800 A mm⁻², respectively. At $t_3 = 7.5$ ms, the temperature of the superconducting layer exceeds the critical temperature of 92 K. As a result, the current completely leaves the superconducting layer and flows exclusively through the metallic layers. This results in a uniform current density in the copper layer ($||\mathbf{J}_{e, Cu}|| = 1000$ A mm⁻²) and no current in the superconducting layer ($||\mathbf{J}_{e. HTS}|| = 0$ A mm⁻²). Subsequently, the magnetic flux density and field lines adopt a more characteristic profile of a conventional coil. Finally, at $t_4 = 30$ s, the temperature of the coil has returned to its initial value of 77 K. Besides the recovery of the operating temperature, there is no more current and magnetic field ensuring a clean start for resuming the tests.

7. Conclusion

A novel coupled FEM – circuit model, referred to as TEFEM – ECM, for simulating the electromagnetic-thermal response of inductive HTS coils under overcurrent tests has been developed. Such inductive coils can be found in inductive fault-current limiters and transformers, for instance. For this model, the ECM makes use of the electromotive force to account for the induction that is not present in purely resistive assembly. It was then efficiently reduced to a simpler model (Coil-Based Model or CBM) which is still representative of the electrical behaviour of the entire inductive coil. Thus, the reduced CBM was validated against experimental data thereby defining its accuracy which is illustrated by a coefficient of determination (R^2) greater than 0.997, while enabling a reduction in computation time of more than a factor of 6 compared with the full LBM (Layer-Based Model). Implementing the CBM, the full TEFEM - ECM was also experimentally validated on the same experimental data. These data were acquired in liquid nitrogen at 77 K. The voltage and the pulsed current experienced by the inductive 2G HTS coil were assessed for pulsed currents of different magnitudes covering different regimes of the superconductor, namely the current sharing regime and the full transition (quench). A very good agreement was observed for the current whereas a fair result was obtained for the coil voltage with a discrepancy resulting from the choice of the convective heat transfer model; the latter being difficult to assess in practice.

This modelling approach presents new opportunities for simulating superconducting devices within increasingly complex electrical networks. Specifically, it enables the simulation of short-circuit scenarios in superconducting motors, transformers, and fault-current limiters integrated with their respective electrical grids.

CRediT authorship contribution statement

Gabriel Hajiri: Conceptualization, Data curation, Formal analysis, Investigation, Writing – original draft, Writing – review & editing. Kévin Berger: Conceptualization, Funding acquisition, Investigation, Methodology, Project administration, Supervision, Validation, Writing – original draft, Writing – review & editing. Frederic Trillaud: Conceptualization, Investigation, Methodology, Validation, Writing – original draft, Writing – review & editing. Jean Lévêque: Investigation, Methodology, Supervision, Validation, Writing – review & editing.

Declaration of competing interest

The authors declare the following financial interests/personal relationships which may be considered as potential competing interests: [Ghazi Hajiri, Kévin Berger and Jean Lévêque reports financial support was provided by BPI France. Ghazi Hajiri, Kévin Berger and Jean Lévêque reports a relationship with BPI France that includes: funding grants].

Acknowledgements

The authors would like to express their gratitude to the French government for funding this work as part of the SuperRail project through BPI France (Banque Publique d'Investissement) under the France 2030 initiative.

F. Trillaud would like to acknowledge the Programa de Apoyo a Proyectos de Investigación e Innovación Tecnológica (PAPIIT) of the Dirección General de Asuntos del Personal Académico (DGAPA) of the Universidad Nacional Autónoma de México (UNAM) under grant PASPA-2024 #IN104124 and the Mexican federal fund, Ciencia básica y de frontera 2023–2024 of the Secretaría de Ciencia, Humanidades, Tecnología e Innovación (Secihti) under the grant CBF2023-2024-2288 for financial support.

Data availability

Data will be made available on request.

References

- [1] Bortot L, Auchmann B, Garcia IC, Gersem HD, Maciejewski M, Mentink M, et al. A coupled A-H formulation for magneto-thermal transients in high-temperature superconducting magnets. IEEE Trans Appl Supercond 2020;30:1–11. https://doi. org/10.1109/TASC.2020.2969476.
- [2] Durante-Gómez W, Trillaud F, dos Santos G, Gonzalez-Montañez F, Hajiri G, Berger K, et al. FEM-Circuit co-simulation of superconducting synchronous wind generators connected to a DC network using the homogenized J-A formulation of the Maxwell equations. Supercond Sci Technol 2024;37:065021. https://doi.org/ 10.1088/1361-6668/ad4a2f.
- [3] Hajiri G, Berger K, Trillaud F, Lévêque J, Caron H. Impact of superconducting cables on a DC railway network. Energies 2023;16:776. https://doi.org/10.3390/ en16020776.
- [4] Wang Y, Song H, Xu D, Li ZY, Jin Z, Hong Z. An equivalent circuit grid model for no-insulation HTS pancake coils. Supercond Sci Technol 2015;28:045017. https:// doi.org/10.1088/0953-2048/28/4/045017.
- [5] Baez-Muñoz A, Trillaud F, Rodriguez-Rodriguez JR, Castro LM, Escarela-Perez R. Reluctance-Based circuit for high-temperature superconductor generator lumped-parameter model. IEEE Trans Magn 2022;58:1–4. https://doi.org/10.1109/ TMAG.2022.3164892.
- [6] Pi W, Liu Z, Li G, Ma S, Meng Y, Shi Q, et al. 4D simulation of quench behavior in quasi-isotropic superconducting cable of stacked REBCO tapes considering thermal contact resistance. Supercond Sci Technol 2020;33:084005. https://doi.org/ 10.1088/1361-6668/ab9aa3.
- [7] dos Santos G, Martins FGR, Sass F, Dias DHN, Sotelo GG, Morandi A. A coupling method of the superconducting devices modeled by finite element method with the lumped parameters electrical circuit. Supercond Sci Technol 2021;34:045014. https://doi.org/10.1088/1361-6668/abe600.
- [8] dos Santos G, Sass F, Sotelo GG, Fajoni F, Baldan CA, Ruppert E. Multi-objective optimization for the superconducting bias coil of a saturated iron core fault current limiter using the T-A formulation. Supercond Sci Technol 2021;34:025012. https://doi.org/10.1088/1361-6668/abc8cf.

- [9] Wang Y, Zheng J, Zhu Z, Zhang M, Yuan W. Quench behavior of high-temperature superconductor (RE)Ba2Cu3Ox CORC cable. J Phys D: Appl Phys 2019;52:345303. https://doi.org/10.1088/1361-6463/ab1e2c.
- [10] Xia Z, Tang Y, Shi J, Ren L, Zhou A, Zhang Y, et al. Verification of HTS SMES lumped parameter network model. IEEE Trans Appl Supercond 2017;27:1–5. https://doi.org/10.1109/TASC.2017.2652861.
- [11] Baez-Muñoz A, Trillaud F, Rodriguez-Rodriguez JR, Castro LM, Escarela-Perez R. Thermoelectromagnetic lumped-parameter model of high temperature superconductor generators for transient stability analysis. IEEE Trans Appl Supercond 2021;31:1–5. https://doi.org/10.1109/TASC.2021.3060696.
- [12] de Sousa WTB, Polasek A, Silva FA, Dias R, Jurelo AR, de Andrade R. Simulations and tests of MCP-BSCCO-2212 superconducting fault current limiters. IEEE Trans Appl Supercond 2012;22:5600106. https://doi.org/10.1109/TASC.2012.2187189.
- [13] Zhou Z, Zhu J, Li H, Qiu M, Li Z, Ding K, et al. Magnetic-Thermal Coupling analysis of the cold dielectric high temperature superconducting cable. IEEE Trans Appl Supercond 2013;23:5400404. https://doi.org/10.1109/TASC.2012.2236377.
- [14] Wang L, Chen Y. An efficient HTS electromagnetic model combining thin-strip, homogeneous and multi-scale methods by T-A formulation. Cryogenics 2022;124: 103469. https://doi.org/10.1016/j.cryogenics.2022.103469.
- [15] Huber F, Song W, Zhang M, Grilli F. The T-A formulation: an efficient approach to model the macroscopic electromagnetic behaviour of HTS coated conductor applications. Supercond Sci Technol 2022;35:043003. https://doi.org/10.1088/ 1361-6668/ac5163.
- [16] Bonnard C-H, Sirois F, Lacroix C, Didier G. Multi-scale model of resistive-type superconducting fault current limiters based on 2G HTS coated conductors. Supercond Sci Technol 2016;30:014005. https://doi.org/10.1088/0953-2048/30/ 1/014005
- [17] Xiang B, Gao L, Liu Z, Geng Y, Wang J. Short-circuit fault current-limiting characteristics of a resistive-type superconducting fault current limiter in DC grids. Supercond Sci Technol 2020;33:024005. https://doi.org/10.1088/1361-6668/ ab6244
- [18] Núñez-Chico AB, Martínez E, Angurel LA, Navarro R. Enhanced quench propagation in 2G-HTS coils co-wound with stainless steel or anodised aluminium tapes. Supercond Sci Technol 2016;29:085012. https://doi.org/10.1088/0953-2048/29/8/085012.
- [19] Zampa A, Lacroix C, Badel A, Sirois F, Tixador P. Current redistribution during inhomogeneous quench of 2G HTS tapes. Supercond Sci Technol 2022;35:095003. https://doi.org/10.1088/1361-6668/ac7c96.
- [20] Chen J, Guan M, Tong Y, Wang X, Zhou Y. Quench detection and early warning based on thermoelastic strain rate for HTS tapes thermally triggered by heat spots. Supercond Sci Technol 2022;36:015013. https://doi.org/10.1088/1361-6668/ 2023/2
- [21] Wang S, Guan M, Chen J, Wang X, Zhou Y. A visual and full-field method for detecting quench and normal zone propagation in HTS tapes. Supercond Sci Technol 2021;35:025010. https://doi.org/10.1088/1361-6668/ac3f9d.
- [22] Marchevsky M, Xie Y-Y, Selvamanickam V. Quench detection method for 2G HTS wire. Supercond Sci Technol 2010;23:034016. https://doi.org/10.1088/0953-2048/23/3/034016.
- [23] Riva N, Sirois F, Lacroix C, de Sousa WTB, Dutoit B, Grilli F. Resistivity of REBCO tapes in overcritical current regime: impact on superconducting fault current limiter modeling. Supercond Sci Technol 2020;33:114008. https://doi.org/10.1088/1361-6668/aba34e.
- [24] Yehia DM, Taha IBM. Application of superconducting fault current limiter as a virtual inertia for DC distribution systems. IEEE Access 2021;9:135384–91. https://doi.org/10.1109/ACCESS.2021.3115989.
- [25] Duron J, Grilli F, Dutoit B, Stavrev S. Modelling the E-J relation of high-Tc superconductors in an arbitrary current range. Physica C 2004;401:231–5. https:// doi.org/10.1016/j.physc.2003.09.044.
- [26] Rhyner J. Magnetic properties and AC-losses of superconductors with power law current—voltage characteristics. Physica C 1993;212:292–300. https://doi.org/ 10.1016/0921-4534(93)90592-E.

- [27] dos Santos Gabriel, de Oliveira Santos Bárbara Maria, Trillaud Frédéric, Hajiri Gabriel, Berger Kévin. T-A-Φ and J-A-Φ formulations for efficient electromagnetic simulations of High-Temperature Superconductors in 2D. Superconductor Science and Technology 2025;38(4):045017. https://doi.org/ 10.1088/1361-6668/adbfc8.
- [28] Santos BMO, Santos GD, Sirois F, Brambilla R, Junior RDA, Sass F, et al. 2-D modeling of HTS coils with T-A formulation: how to handle different coupling scenarios. IEEE Trans Appl Supercond 2022;32(5):1–4. https://doi.org/10.1109/ TASC.2022.3160512.
- [29] Friedmann TA, Rabin MW, Giapintzakis J, Rice JP, Ginsberg DM. Direct measurement of the anisotropy of the resistivity in the a-b plane of twin-free, single-crystal, superconducting YBa₂Cu₃O₇₋₈. PhysRevB 1990;42:6217–21. https:// doi.org/10.1103/PhysRevB.42.6217.
- [30] Kim YB, Hempstead CF, Strnad AR. Critical persistent currents in hard superconductors. PhysRevLett 1962;9:306–9. https://doi.org/10.1103/ PhysRevLett 9 306
- [31] Wimbush SC, Strickland NM. A public database of high-temperature superconductor critical current data. IEEE Trans Appl Supercond 2017;27:1–5. https://doi.org/10.1109/TASC.2016.2628700.
- [32] Schönborg N, Hörnfeldt S. Model of the temperature dependence of the hysteresis losses in a high-temperature superconductor. Physica C 2002;372–376:1734–8. https://doi.org/10.1016/S0921-4534(02)01113-9.
- [33] dos Santos G, Trillaud F, Santos BMO, Sass F, Sotelo GG. Fast coupled thermoelectric and magnetic model to simulate the transient behavior of inductive and resistive superconducting fault-current limiters. IEEE Trans Appl Supercond 2024;34:1–17. https://doi.org/10.1109/TASC.2023.3332553.
- [34] Ekin J. Experimental techniques: cryostat design, material properties and superconductor critical-current testing. 1st edition. Oxford: Oxford University Press: 2006.
- [35] M\u00e4der O. Simulationen und Experimente zum Stabilit\u00e4tsverhalten von HTSL-Bandleitern. KIT Scientific Publishing 2012. https://doi.org/10.5445/KSP/ 1000028713.
- [36] Merte H. Incipient and steady boiling of liquid nitrogen and liquid hydrogen under reduced gravity 1970.
- [37] Berger AD. Stability of superconducting cables with twisted stacked YBCO coated conductors 2011.
- [38] Jin T, Hong J, Zheng H, Tang K, Gan Z. Measurement of boiling heat transfer coefficient in liquid nitrogen bath by inverse heat conduction method. J Zhejiang Univ Sci A 2009;10:691–6. https://doi.org/10.1631/jzus.A0820540.
- [39] de Sousa WTB, Polasek A, Dias R, Matt CFT, de Andrade R. Thermal–electrical analogy for simulations of superconducting fault current limiters. Cryogenics 2014; 62:97–109. https://doi.org/10.1016/j.cryogenics.2014.04.015.
- [40] Yazdani-Asrami M, Staines M, Sidorov G, Eicher A. Heat transfer and recovery performance enhancement of metal and superconducting tapes under high current pulses for improving fault current-limiting behavior of HTS transformers. Supercond Sci Technol 2020;33:095014. https://doi.org/10.1088/1361-6668/ abs542
- [41] Yazdani-Asrami M, Staines M, Sidorov G, Davies M, Bailey J, Allpress N, et al. Fault current limiting HTS transformer with extended fault withstand time. Supercond Sci Technol 2019;32:035006. https://doi.org/10.1088/1361-6668/aaf7a8.
- [42] Grover FW. Inductance calculations: working formulas and tables. Mineola, N.Y. Dover Publications: 2004.
- [43] dos Santos G, Trillaud F. A frequency-domain finite element model for simulating high temperature superconductors using the J-A and T-A formulations. Supercond Sci Technol 2024;37:115016. https://doi.org/10.1088/1361-6668/ad8141.
- [44] Trillaud F, dos Santos G, Gonçalves SG. Essential material knowledge and recent model developments for REBCO-coated conductors in electric power systems. Materials 2021;14:1892. https://doi.org/10.3390/ma14081892.